J. Fluid Mech. (1992), *vol.* 240, *pp.* 229–258
Printed in Great Britain

Zero-Prandtl-number convection

By OLIVIER THUAL†
National Center for Atmospheric Research, PO Box 3000, Boulder, CO 80307, USA

(Received 20 August 1991 and in revised form 30 December 1991)

The zero-Prandtl-number limit of the Oberbeck–Boussinesq equations is compared to small-Prandtl-number Rayleigh–Bénard convection through numerical simulations. Both no-slip and free-slip boundary conditions, imposed at the top and bottom of a small-aspect-ratio, horizontally periodic box are considered. A rich variety of regimes is observed as the Rayleigh number is increased: supercritical oscillatory instabilities for various values of the aspect ratios, competition between two-dimensional rolls, squares and hexagonal patterns, competition between travelling and standing waves, transition to chaos, and scalings laws for the first Rayleigh-number decade. This multiplicity of regimes can be attributed to the close interaction between the stationary and oscillatory instabilities at zero Prandtl number.

1. Introduction

1.1. *Geophysics, turbulence, and nonlinear dynamics*

The study of thermal convection at very low Prandtl number has long been motivated by geophysical and astrophysical interests. The Earth's liquid-core convection is thought to be governed by a Prandtl number of order $P \sim 0.1$, owing to the metallic nature of its materials. The Prandtl number in the convection zone of the sun and stars is extremely small ($P \sim 10^{-8}$) owing to the effective conductivity governed by radiative processes. The large value of the conductivity prevents motions from distorting the mean temperature profile, and convection is not an efficient mode of heat transport, even for strong forcing. The solar granulation shows a non-stationary, irregular pattern of roughly polygonal cells.

In the astrophysical context, an asymptotic form of the Oberbeck–Boussinesq equations in the zero-Prandtl-number limit have been derived by Spiegel (1962). The asymptotic expansion which leads to these equations is presented here in §2. Concerns about the compatibility of this limit with the Boussinesq approximation have been raised (S. Fauve 1985, personal communication). But even if the compressibility of the stellar fluids must be taken into account to describe accurately the convective zone of the sun, these zero-Prandtl-number equations provide a good model for turbulence studies (Spiegel 1962; Kraichnan & Spiegel 1962; Herring 1987). These equations are indeed the Navier–Stokes equations with an intrinsic forcing at large scales (analogous to the Kuramoto–Sivashinsky equations).

Finally, the study of small-Prandtl-number convection can be justified for the insight it may shed into nonlinear dynamics. The investigation of instabilities in Rayleigh–Bénard convection has contributed to a large amount of theoretical progress in nonlinear dynamics. A systematic study of the stability of stationary

† Present address: CERFACS, 42 Av. Coriolis, 31057 Toulouse Cedex, France.

convective patterns has been conducted for several years by Busse and his collaborators (Schlüter, Lortz & Busse 1965; Busse 1967, 1971, 1972; Busse & Clever 1979, 1981; Clever & Busse 1974, 1978, 1981, 1987, 1989, 1990; Busse & Bolton 1984; Bolton & Busse 1985; Bolton, Busse & Clever 1986; see also the reviews by Busse 1978, 1981, 1989). When the Prandtl number becomes small, it is observed that the secondary instabilities approach the onset of convection at the critical Rayleigh number $R = R_c$. This onset, for instance, becomes coincident with the oscillatory instability of the two-dimensional roll pattern as the Prandtl number tends to zero and for free-slip boundary conditions (Busse 1972). A brief review of this progress is made here, in §3, by focusing on the results which are pertinent for the present study.

The merging or at least the confluence of these instabilities at zero Prandtl number is an appropriate situation for the application of the nonlinear dynamics theory based on symmetry considerations and asymptotic expansions, such as amplitude or phase equations (see, for instance, Newell, Passot & Soul 1990 for a recent review). These powerful analytical tools should be able to describe the likely numerous regimes concentrated near the onset of convection and solutions of the zero- and small-Prandtl-number equations.

1.2. *Experiments, theory and numerical simulations*

One successful aspect of the study of instabilities in Rayleigh–Bénard convection is the good agreement of theory with experiments. Low-Prandtl-number fluids exhibit interesting convective patterns and well-controlled transitions to chaos (see Croquette 1989*a*, *b* for a review). However, very small Prandtl number cannot be achieved in the laboratory, and small-Prandtl-number fluids, like mercury with $P = 0.025$, do not allow good visualization of the convective patterns.

This reinforces the role of numerical simulations as an experimental tool for the exploration of small-Prandtl-number convection. Direct numerical simulations have given good support for significant theoretical developments (Siggia & Zippelius 1981; Zippelius & Siggia 1982, 1983; Busse & Bolton 1984; Bolton & Busse 1985). Early simulations of chaotic regimes, bifurcated from the oscillatory instability have been performed by Lipps (1976) and McLaughlin & Orszag (1982). All simulations suggest that stable travelling waves bifurcate supercritically at $R = R_{II}$ from the two-dimensional roll pattern. For the case of no-slip boundary conditions, Clever & Busse (1987, 1989, 1990) found that these travelling waves encounter a secondary bifurcation at $R = R_{III}$ which saturate on a quasi-periodic regime. The same phenomena have been observed for free-slip boundary conditions by Tveitereid, Palm & Skogvang (1986) and Meneguzzi *et al.* (1987). The subsequent transition to chaos is achieved through the appearance of a third frequency.

Several numerical studies have investigated two-dimensional or axisymmetric convective rolls at very small Prandtl number and predicted the zero-Prandtl-number behaviour through an extrapolation (Jones, Moore & Weiss 1976; Proctor 1977; Clever & Busse 1981; Busse & Clever 1981). These works, reinforced by experimental observations (Chiffaudel, Fauve & Perrin 1987), show that a viscous regime just above the onset of convection is followed by an inertial regime where the convective motion tends to be a rigid rotation near the axis of the convective roll (the 'flywheel effect'). This flow pattern tends to annihilate the advection term of the momentum equation leading to drastic intensification of the convection for very low Prandtl numbers. This challenging problem of inertial convection is addressed in Clever & Busse (1990) who also point out that the two-dimensional solution for inertial convection is unstable with respect to three-dimensional instabilities.

One of the major limitations of these numerical studies at low Prandtl number is the large discrepancy between the viscous and diffusive timescales (P is their ratio). The asymptotic limit leading to the zero-Prandtl-number equations of §2 allows one to get rid of this stiffness problem. These equations have been simulated by Herring (1970) for free-slip boundary conditions. He reported blow-up behaviour for a large class of initial conditions, which can be understood by the fact that the nonlinear terms of these equations vanish identically for the two-dimensional-roll modes. For no-slip boundary conditions, Clever & Busse (1990) have compared the first instabilities of these zero-Prandtl-number equations to those of very low Prandtl numbers. They have shown that the limit of vanishing Prandtl number is approached smoothly in the range of Rayleigh numbers that includes at least two subsequent bifurcations beyond the onset of convection. These two studies are at the root of the present work.

1.3. *The present experiment*

Three numerical spectral codes with periodically horizontal boundary conditions are described in §4, and used in the present experiment. Two of them (SST and KER) allow no-slip boundary conditions at the top and bottom of the layer and use two different spectral methods. The third one (THU), written for this study, allows free-slip boundary conditions. All these codes have been adapted to handle cases of both finite or zero Prandtl number.

Numerical experiments for no-slip boundary conditions are reported in §5. It is shown that the two cases, $P = 0$ and 0.025, are very close to each other, at least for the first instabilities. To check a theoretical prediction by Fauve, Bolton & Brachet (1987), various values of the aspect ratios of the box, k_x and k_y, have been explored; the oscillatory instability of the two-dimensional convective rolls is always supercritical, and leads to stable travelling waves. The next instability at $R = R_{III}$ does not follow the picture described by Clever & Busse (1987, 1989, 1990) and leads to stable standing waves instead of a quasi-periodic regime. But the choice $k_x = 3.117$ and $k_y = 2.2$ in the present experiment may explain this discrepancy. The subsequent transition to chaos from this regime is briefly documented here, with focus on intermittent regimes involving both a convective roll and a polygonal pattern. Attention is paid to scaling laws of the Nusselt number and energies on the first decade of variation of the Rayleigh number.

The case of free-slip boundary conditions in a square box of aspect ratio $k_x = k_y = \pi/\sqrt{2}$ is investigated in §6 with the new code THU. For finite Prandtl number $P = 0.2$, the competition between travelling waves and standing waves leads to a bifurcation diagram similar to the case of no-slip boundary conditions and to a transition to chaos consistent with Meneguzzi *et al.* (1987). Surprisingly, at $P = 0$, the system did not blow up, except when starting exactly with the two-dimensional-roll marginal mode. Square or hexagon patterns are selected instead of the two-dimensional convective rolls which go to infinity as $P \to 0$. By varying the Prandtl number continuously from 0 to 0.2, it is shown that these patterns are the proper limits of some small-Prandtl-number, stable solutions. The multiplicity of solutions in this region of the control space prevents a complete investigation of the bifurcation diagram; only the main regimes and patterns are presented here.

As this work is the only one after Herring (1970) and Clever & Busse (1990) to investigate the zero-Prandtl-number equations, it cannot report a complete and exhaustive study of their solutions. In particular, it does not explore large aspect ratios. Given a finite amount of computer time, only the principal regimes observed in numerous but finite numerical experiments are reported here. But their

multiplicity and variety suggest that these zero-Prandtl-number equations are an interesting model for the study of instabilities.

2. Zero-Prandtl-number equations

2.1. *The Boussinesq approximation*

A horizontal layer of fluid of thickness d is heated from below by imposing the temperatures T_1 and T_2 at the bottom and upper horizontal conductive plates. When d is not too large, the fluid motion can be described by the Boussinesq approximation (Spiegel & Veronis 1960) leading to the Oberbeck–Boussinesq equation:

$$\left.\begin{aligned} \boldsymbol{v}_t + \boldsymbol{v}\cdot\boldsymbol{\nabla}\boldsymbol{v} &= -\frac{\boldsymbol{\nabla} p}{\rho_0} + \nu\nabla^2\boldsymbol{v} + g\frac{\rho}{\rho_0}\boldsymbol{e}_3, \\ \boldsymbol{\nabla}\cdot\boldsymbol{v} &= 0, \\ T_t + \boldsymbol{v}\cdot\boldsymbol{\nabla} T &= \kappa\nabla^2 T, \end{aligned}\right\} \tag{2.1}$$

where $\boldsymbol{v} = (u, v, w)$ is the velocity, T the temperature, ρ the density, p the pressure, $\boldsymbol{e}_3$ the vertical unit vector, g the acceleration due to gravity, ν the viscosity, and κ the temperature conductivity. The equation of state is linear, $\rho = \rho_0[1-\alpha(T-T_0)]$, with α the thermal expansion coefficient and ρ_0 and T_0 reference density and temperature.

If one choses units d for length, d^2/ν for time (thus ν/d for velocity), $\nu/\kappa(T_1-T_2)$ for temperature, and a convenient unit for the pressure, the dimensionless Oberbeck–Bousinesq equations read

$$\left.\begin{aligned} \boldsymbol{v}_t + \boldsymbol{v}\cdot\boldsymbol{\nabla}\boldsymbol{v} &= -\boldsymbol{\nabla} p + \nabla^2\boldsymbol{v} + R\theta\,\boldsymbol{e}_3, \\ \boldsymbol{\nabla}\cdot\boldsymbol{v} &= 0, \\ P(\theta_t + \boldsymbol{v}\cdot\boldsymbol{\nabla}\theta) &= w + \nabla^2\theta, \end{aligned}\right\} \tag{2.2}$$

where w is the vertical component of the velocity and $\theta = T(x, y, z) - T_{\mathrm{d}}(z)$ is the temperature deviation from the linear diffusive profile $T_{\mathrm{d}}(z)$. The dimensionless control parameters are the Rayleigh number $R = \alpha g d^3(T_1-T_2)/\nu\kappa$, the Prandtl number $P = \nu/\kappa$, and the two aspect ratios $k_x = 2\pi d/L_x$ and $k_y = 2\pi d/L_y$, where L_x and L_y are the horizontal dimensions of the box.

Periodicity of all fields is assumed in the horizontal direction. In the vertical direction, the temperature boundary conditions read $\theta = 0$ at $z = 0$ and $z = 1$. Two types of boundary conditions for the velocity are considered. For the no-slip boundary conditions $\boldsymbol{v} = 0$ at $z = 0$ and $z = 1$, and for the free-slip boundary conditions $\partial_z u = \partial_z v = 0$ at $z = 0$ and $z = 1$.

2.2. *The zero-Prandtl-number limit*

Let us denote the dimensionless form of (2.2.) by the four dimensionless numbers

$$\begin{pmatrix} 1 & R \\ P^{-1} & P^{-1} \end{pmatrix}$$

which are in front of the terms

$$\begin{pmatrix} \nabla^2\boldsymbol{v} & \theta\boldsymbol{e}_3 \\ w & \nabla^2\theta \end{pmatrix},$$

with the convention that the terms on the left-hand sides of these equations have coefficients equal to one. The units for the pressure are unimportant because the term

∇p is only a constraint to maintain the incompressibility. If we keep the unit of length equal to d but multiply the unit of velocity by an arbitrary factor $W(R,P)$ (and thus divide the unit of time by the same factor) and the unit of temperature by an arbitrary $\Theta(R,P)$, the new dimensionless form of the Boussinesq equations now reads

$$\begin{pmatrix} W^{-1} & R\Theta W^{-2} \\ P^{-1}\Theta^{-1} & P^{-1}W^{-1} \end{pmatrix}.$$

For instance, the choices $W = P^{-1}$ and $\Theta = P^{-1}R^{-1}$ lead to the dimensionless form

$$\begin{pmatrix} P & P \\ R & 1 \end{pmatrix}$$

which is widely used in the literature.

Examining asymptotic solutions of the Boussinesq equations in the limit $P \to 0$ requires an assumption on the leading behaviour of the velocity $v = W(P)[v^{(0)} + Pv^{(1)} + O(P^2)]$ and the temperature $\theta = \Theta(P)[\theta^{(0)} + P\theta^{(0)} + O(P^2)]$, where the $v^{(i)}$ and $\theta^{(i)}$ are of order 1 and the functions W and Θ express the leading behaviour of the velocity ($W = P^{\gamma}$) and the temperature ($\Theta = P^{\delta}$). Keeping a dimensionless form of the equations and examining all the dominant balances of terms in the equations (by exploring all the possible W and Θ) is equivalent to changing the dimensionless form of the equations and assuming that the fields v and θ, expressed in the new units, are of order 1 when $P \to 0$.

For instance, if $W = \Theta = P^{-1}$, the dimensionless form

$$\begin{pmatrix} P & RP \\ 1 & 1 \end{pmatrix}$$

equations read

$$\begin{pmatrix} 0 & 0 \\ 1 & 1 \end{pmatrix}$$

for $P = 0$, i.e. a three-dimensional (3D) Euler equation decoupled from a temperature equation forced by a vertical velocity term. The order-one solutions of these 3D Euler equations scale like P^{-1} in the original dimensionless form of (2.2). These asymptotic equations describe solutions issued from initial conditions which are so strong that the viscosity and the buoyancy play no role, or from initial conditions which tend to blow up (e.g. because of the 'fly-wheel effect'). Another example is obtained by choosing $W = P^{-1}$ and $\Theta = P^{-2}$, leading to the dimensionless form

$$\begin{pmatrix} P & R \\ P & 1 \end{pmatrix}$$

and the asymptotic equations

$$\begin{pmatrix} 0 & R \\ 0 & 1 \end{pmatrix},$$

i.e. a heat equation decoupled from a 3D Euler equation forced by the buoyancy. But these asymptotics only describe a transient because there is no forcing in these asymptotic equations, and the temperature diffusion damps the temperature which will eventually stop scaling as P^{-2}. A third non-trivial dominant balance is obtained for $W = 1$ and $\Theta = P$, which leads to an (x,y) two-dimensional (2D) Navier–Stokes

equation with no forcing term, and the constraint $w = 0$. This asymptotic equation actually describes particular solutions of (2.2) issued from 2D initial conditions with small deviation from the conductive profile.

The present work is concerned with the scaling $W = \Theta = 1$, i.e. with order-one solutions of (2.2). For $P = 0$ these order-one solutions are described by the asymptotic equations

$$\left.\begin{aligned} \boldsymbol{v}_t + \boldsymbol{v}\cdot\boldsymbol{\nabla}\boldsymbol{v} &= -\boldsymbol{\nabla}p + \boldsymbol{\nabla}^2\boldsymbol{v} + R\theta\,\boldsymbol{e}_3, \\ \boldsymbol{\nabla}\cdot\boldsymbol{v} &= 0, \\ 0 &= w + \nabla^2\theta. \end{aligned}\right\} \tag{2.3}$$

The inversion $\theta = \nabla^{-2}w$ with the boundary conditions $\theta = 0$, at $z = 0$ and $z = 1$, and the horizontal periodicity of the temperature is a well-posed problem.

These asymptotic equations have been derived by Spiegel (1962), but in his formalism the first order in the temperature expansion is a null term, so that (2.3) seems to appear only at the second order. However the asymptotic derivation of (2.3) can be rephrased as has been done in this section.

2.3. *The Nusselt number*

Taking the horizontal average of the temperature equation in (2.1), i.e. the Oberbeck–Boussinesq equations with physical units, and examining stationary solutions lead to the z ordinary differential equation $\partial_z\langle wT\rangle^{xy} = \kappa\partial_z^2\langle T\rangle^{xy}$, where the horizontal average of 3D field $f(x, y, z)$ is defined by

$$\langle f\rangle^{xy}(z) = \frac{1}{L_x}\frac{1}{L_y}\int_0^{L_x}\int_0^{L_y} f(x, y, z)\,\mathrm{d}x\,\mathrm{d}y.$$

The integration constant

$$H = -\kappa\partial_z\langle T\rangle^{xy}(z) + \langle wT\rangle^{xy}(z)$$

is the heat flux. By choosing $z = 0$ and $z = d$ in this z-dependent expression, and using the boundary condition $w = 0$, this constant can be viewed as minus the slope of the mean temperature profile near the plates times the diffusivity;

$$H = -\kappa\partial_z\langle T\rangle^{xy}(0) = -\kappa\partial_z\langle T\rangle^{xy}(d).$$

Another interesting expression of the heat flux is obtained by averaging its z-dependent expression in the vertical to get

$$H = -\kappa\langle\partial_z T\rangle^{xyz} + \langle wT\rangle^{xyz} = \kappa\frac{T_2 - T_1}{d} + \langle wT\rangle^{xyz},$$

where the vertical averaging is defined by

$$\langle f\rangle^{z} = \frac{1}{d}\int_0^d f(z)\,\mathrm{d}z.$$

When there is no convection the heat flux is simply $H_0 = \kappa(T_1 - T_2)/d$. The Nusselt number is by definition the ratio $Nu = H/H_0$ of the actual flux H over the conductive flux H_0, i.e.

$$Nu = 1 + d\frac{\langle wT\rangle^{xyz}}{\kappa(T_1 - T_2)}.$$

Switching to the dimensionless quantities $x, y, z, \boldsymbol{v}$, and θ, the expression for the Nusselt number reads

$$Nu = 1 + P^2 \langle w\theta \rangle^{xyz}. \tag{2.4}$$

The same expression could have been obtained directly from the dimensionless equations (2.2) by taking into account the fact that the dimensionless temperatures imposed on the plates are equal to $T_1/P(T_1 - T_2)$ and $T_2/P(T_1 - T_2)$.

Order-one solutions of the asymptotic equations (2.3) are characterized by a Nusselt number identically equal to one. Physically, this is because the mean profile of temperature in the layer is equal to the conductive profile. However, $E_{w\theta} = \langle w\theta \rangle^{xyz}$ is an interesting quantity to measure for zero-Prandtl-number convection, as it is the coefficient of the leading order of $Nu - 1$ in the limit $P \to 0$.

For time-dependent regimes, these various expressions of the heat flux and the Nusselt number are identical to the case of stationary solutions, provided that a time average is performed. The definition of the Nusselt number reads

$$Nu = 1 + P^2 \langle w\theta \rangle^{xyzt}, \tag{2.5}$$

and the mean value of $E_{w\theta}(t)$ is the interesting quantity to measure at zero Prandtl numbers.

2.4. *The poloidal–toroidal decomposition*

The elimination of pressure in the Oberbeck–Bousinesq equations can be done using the poloidal–toroidal decomposition of the velocity field $\boldsymbol{v} = (u, v, w)$:

$$\begin{aligned} \boldsymbol{v}(x, y, z) &= \boldsymbol{\nabla} \times [\boldsymbol{\nabla} \times \phi(x, y, z)\, \boldsymbol{e}_3] + \boldsymbol{\nabla} \times \psi(x, y, z)\, \boldsymbol{e}_3 + \boldsymbol{U}(z) \\ &= (\phi_{xz} + \psi_y + U, \phi_{yz} - \psi_x + V, -\nabla_H^2 \phi), \end{aligned} \tag{2.6}$$

where $\nabla_H^2 = \partial_x^2 + \partial_y^2$ is the horizontal Laplacian. This decomposition has often been used in studies of Rayleigh–Bénard convection. However, the introduction of the mean shear $\boldsymbol{U}(z) = [U, V]$ had sometimes been forgotten (e.g. Clever & Busse 1987), even for convective regimes where it was not negligible. Its importance has been realized recently by Clever & Busse (1989), who corrected their previous results accordingly.

Projecting on the vertical direction $\boldsymbol{e}_3$ the curl and the (curl)^2 of the momentum equation, the evolution equation for vertical vorticity $\zeta(x, y, z, t) = -\nabla_H^2 \psi$, the vertical velocity $w(x, y, z, t) = -\nabla_H^2 \phi$, the temperature deviation $\theta(x, y, z, t)$, and the two mean shear components $U(z, t)$ and $V(z, t)$ read

$$\left.\begin{aligned} \zeta_t + N_1(\boldsymbol{v} \cdot \boldsymbol{\nabla} \boldsymbol{v}) &= \nabla^2 \zeta, \\ \nabla^2 w_t - N_2(\boldsymbol{v} \cdot \boldsymbol{\nabla} \boldsymbol{v}) &= R \nabla_H^2 \theta + \nabla^4 w, \\ P(\theta_t + \boldsymbol{v} \cdot \boldsymbol{\nabla} \theta) &= w + \nabla^2 \theta, \\ U_t + \partial_z \langle uw \rangle^{xy} &= U_{zz}, \\ V_t + \partial_z \langle vw \rangle^{xy} &= V_{zz}, \end{aligned}\right\} \tag{2.7}$$

where N_1 and N_2 are the nonlinear projections

$$N_1(\boldsymbol{f}) = \boldsymbol{e}_3 \cdot \boldsymbol{\nabla} \times \boldsymbol{f} \text{ and } N_2(\boldsymbol{f}) = \boldsymbol{e}_3 \cdot \boldsymbol{\nabla} \times (\boldsymbol{\nabla} \times \boldsymbol{f}),$$

and $\langle f \rangle^{xy}(z)$ denotes the horizontal average of a field $f(x, y, z)$.

The system (2.6), (2.7), with the horizontally periodic boundary conditions, and either no-slip boundary conditions or free-slip boundary conditions is well posed.

Knowledge of ζ and w defines ψ and f up to an arbitrary field $G(z)$, which is actually a gauge of the decomposition and plays no role in the value of $\boldsymbol{v}$.

3. Instabilities at small Prandtl numbers

3.1. *The importance of multiple instabilities*

A complete understanding of the transition to chaos, and to fully developed turbulence, for small and zero Prandtl numbers would consist in detailing all the bifurcations which occur in the control space of the parameters (P, R, k_x, k_y), including the large-aspect-ratio limits $k_x \to 0$ and $k_y \to 0$, for both no-slip and free-slip boundary conditions. Such a task is, of course, beyond computer and human capabilities. Nevertheless, numerical experiments, such as the ones presented here, are useful to discover the principal regimes that dominate these transitions to chaos and fully developed turbulence. A first step toward the understanding of these transitions can be started by a theoretical investigation of some observed simple bifurcations, such as the stationary or the oscillatory instabilities, or some non-generic multiple instabilities obtained for specific values of the control parameters. Indeed, most of the regimes observed in the transition have roots in such instabilities through stable or unstable bifurcated solutions.

The theory of instabilities is now at an advanced stage where it is possible to perform numerous predictions using only the symmetries of the equations and of the bifurcating regimes. Symmetry considerations are useful to derive *a priori* the amplitude equations valid in the vicinities of instabilities (e.g. Golubitsky, Stewart & Schaeffer 1988). The addition of higher-order terms in these amplitude equations, and the study of some degenerate cases in the values of the nonlinear coefficients, often describe the secondary instabilities (see Crawford & Knobloch 1991).

In the following section, only selected results, pertinent to the interpretation of the present numerical experiments in low-aspect-ratio boxes, are reviewed.

3.2. *The onset of convection*

The stability of the conductive state can be solved analytically for horizontal periodic conditions (see Chandrasekhar 1961). The onset of convection is a stationary instability (also called the 'exchange of stability principle') independent of the Prandtl number. The critical values are $R_c \sim 1707$, $k_c \sim 3.117$ for no-slip boundary conditions and $R_c = 27\pi^4/4 \sim 657$, $k_c = \pi/\sqrt{2} \sim 2.22$ for free-slip boundary conditions. At the onset of convection, each wave vector $\boldsymbol{q}$ whose modulus $|\boldsymbol{q}|$ is equal to k_c, is associated with a marginal mode $X = A\Phi(z)\exp \mathrm{i}\boldsymbol{q}\boldsymbol{x} + (*)$, complex conjugated, where the velocity and temperature are the components of X, and the profile $\Phi(z)$ depends on the nature of the boundary conditions (free-slip or rigid). The nonlinear saturation of the amplitude of such a single 2D convection roll is governed, near the onset and at the leading order in A, by the amplitude equation (Landau equation)

$$\dot{A} = \mu A + \lambda |A|^2 A, \tag{3.1}$$

where μ is proportional to $R - R_c$.

Any pattern obtained with a linear combination of marginal modes

$$X = \sum_{j=1}^{N} A_j \Phi(z) \exp \mathrm{i}\boldsymbol{q}_j \boldsymbol{x} + (*), \tag{3.2}$$

with $|\boldsymbol{q}_j| = k_c$, is likely to be a bifurcated solution. The amplitude equation governing the nonlinear competition of these N marginal modes reads

$$\dot{A}_j = \mu A_j + \sum_{l=1}^{N} \lambda_{jl} |A_l|^2 A_j. \tag{3.3}$$

If the wave vectors $\boldsymbol{q}_j$ are regularly distributed on the circle of radius k_c, square patterns are obtained for $N = 2$, hexagons for $N = 3$, and so on.

The numerical values of the nonlinear coefficients of these amplitude equations have been documented in the literature (e.g. Schlüter *et al.* 1965; Malkus & Veronis 1958; Cross 1980; Daniels & Ong 1990). It can be proven that 2D convection rolls are always selected in a supercritical manner, at least for finite Prandtl numbers. By adding the next-order nonlinear terms of the amplitude equations (3.1) or (3.2), and looking at degenerate cases for the values of their coefficients, the competition between various patterns (e.g. rolls, squares, and hexagons) and their secondary bifurcations can be classified (Golubitsky, Swift & Knobloch 1984; Crawford & Knobloch 1991).

3.3. *Secondary instabilities and large-aspect-ratio limits*

Studying instabilities in the large-aspect-ratio limit $k_x \to 0$ and $k_y \to 0$ can be useful to explain secondary instabilities of convection patterns which are pertinent to the low-aspect-ratios cases. In a horizontally infinite layer, discrete modes are replaced by continua of modes, and the amplitudes $A_j(t)$ of (3.1) or (3.2) must be replaced by $A_j(x, y, t)$ which are the slowly varying envelope describing a wave packet of quasi-marginal modes. A good review of the amplitude-equation approach applied to convection can be found in the introduction of Newell *et al.* (1990).

In the case of wave packets of 2D rolls, Newell & Whitehead (1969) and Segel (1969) have derived the partial derivative equations for the amplitude $A(x, y, t)$. Secondary instabilities pertinent for large aspect ratios (e.g. the Eckhaus and the skew-varicose instabilities) as well as for small aspect ratios (e.g. the zigzag instability) are contained in these equations. Subsequently, Siggia & Zippelius (1981) noticed that these amplitude equations were not complete because they ignored a marginal mode which is associated with a slowly varying vertical vorticity. The new set of amplitude equations, including the vorticity mode amplitude, predicts that, for small Prandtl numbers, 2D convective rolls are always unstable in an infinite layer (Zippelius & Siggia 1982, 1983). It also contains new secondary instabilities such as the oscillatory instability, pertinent for low aspect ratios. However, the work of Zippelius & Siggia did not capture the actual secondary instabilities of convection for free-slip boundary conditions, because it included some restrictive assumptions about the wavenumbers of the disturbances. This flaw is corrected by the analytical study of Busse & Bolton (1984) which is validated by the numerical simulations of Bolton & Busse (1985). To complete the hierarchy of amplitude equations, one should also include the coupling with the mean shears $U(z)$, which are not represented by the vertical vorticity component, to see whether new secondary instabilities could be obtained.

Most of the secondary instabilities of convective patterns can be interpreted as phase instabilities. Such an interpretation can be found in Fauve *et al.* (1986) or Newell *et al*, (1990). The primary instability breaks some symmetries, e.g. the translational or Galilean invariances. Instead of one solution (the conductive state) invariant under these symmetries, the bifurcated stationary patterns describe orbits of solutions when these symmetries are applied. This implies that there exists a

marginal mode for the stability of these patterns, which can be at the root of a continuum of quasi-marginal modes, possibly unstable. The nonlinear dynamics of such instabilities can be described by phase equations. These phase equations can easily be obtained from the amplitude equations of the primary instabilities, if these contain the desired secondary instability, or directly from the original equations. As for amplitude equations, symmetry considerations can predict the form of the phase equations.

3.4. *The oscillatory instability*

The onset of the oscillatory instability of 2D rolls for low Prandtl numbers has been extensively documented in the literature (Busse 1972; Clever & Busse 1974, 1978, 1981; Busse & Bolton 1984; Bolton & Busse 1985; Bolton *et al.* 1986). The saturation of this instability to a stable travelling-wave regime has been observed in many laboratory experiments (see Croquette 1989*a*, *b*) and numerical simulations (e.g. Clever & Busse 1987, 1989, 1990; Meneguzzi *et al.* 1987), covering a wide variety of parameters.

The form of the amplitude equations of the oscillatory instability of the 2D convective rolls in a small-aspect-ratio box can be derived with symmetry arguments (translations in the x-direction). Let $Y = W_r\,\Psi(x,z)\exp \mathrm{i}py + W_l\,\Psi^*(x,z)\exp \mathrm{i}py + (*)$ denote the marginal mode of this instability, where Ψ depends on the boundary conditions and p on the aspect ratios. The amplitude equations read

$$\left.\begin{aligned} \dot{W}_r &= (\mu + \mathrm{i}\omega)\,W_r + (\lambda_1|W_r|^2 + \lambda_2|W_l|^2)\,W_r, \\ \dot{W}_l &= (\mu - \mathrm{i}\omega)\,W_l + (\lambda_1|W_l|^2 + \lambda_2|W_r|^2)\,W_l, \end{aligned}\right\} \tag{3.4}$$

where μ is proportional to $R - R_{\mathrm{II}}$, and ω is the oscillatory frequency.

A discussion on the values of the nonlinear coefficient allows one a classification to see whether travelling waves, with one of the two amplitudes vanishing, or the standing waves, with $|W_r| = |W_l|$, are selected. The only attempts to calculate the actual values of these coefficients for free-slip boundary conditions and no-slip boundary conditions have been made by Fauve *et al.* (1987) with a phase-theory approach. For free-slip boundary conditions, the oscillatory instability is due to the interaction of the x-translational and x-Galilean invariances of the basic 2D pattern; the phase equation can be derived exactly from the linear stability analysis. It predicts a supercritical bifurcation leading to stable travelling waves. For no-slip boundary conditions, such an exact calculation is no longer possible; Fauve *et al.* (1987) proposed a model by including a dissipation term in the phase equations to mimic the effect of the no-slip boundaries. This model predicts supercritical instabilities for aspect ratios k_x around the critical value $k_c = 3.117$, but also subcriticality for small Prandtl numbers and values of the aspect ratio k_x smaller than a specified threshold. This prediction is investigated numerically in §5.

As for the stationary instabilities, the instabilities of the periodic regimes bifurcated from an oscillatory instability can be classified a priori by adding more nonlinear terms in the amplitude equation (3.3) and looking at degenerate values of their coefficients (see Crawford & Knobloch 1991). The bifurcation diagrams for the competition between travelling waves and standing waves observed in §5 can be recognized as one case of this classification.

3.5. *The zero-Prandtl-number limit*

For free-slip boundary conditions in the limit $P = 0$, the nonlinear term coefficient λ of the amplitude equation of the (3.1) 2D roll vanishes. Actually, all the nonlinear terms, at every order, also vanish, as can be deduced from the asymptotic

Oberbeck–Boussinesq equations (2.3); the nonlinear term is indeed zero for the 2D marginal mode. This implies that there exists a trajectory of the unstable manifold of the conductive state, in the phase space of (2.3), which goes to infinity. Contrary to the case of finite Prandtl number or rigid boundary conditions, other patterns like squares or hexagons are likely to be selected at $P = 0$. Indeed, for the case of free-slip boundary conditions, the amplitude of the 2D roll pattern goes to infinity when $P \to 0$, while other patterns remain finite. This result does not contradict the analysis of Schlüter *et al.* (1965) which uses a dimensionless form of equations different from the one of (2.2).

In the limit $P \to 0$ and $k_y \to 0$, the stationary and oscillatory instabilities occur simultaneously. It is beyond the scope of this work to write and to study the amplitude equation corresponding to this interaction between these two instabilities, but such an approach is likely to be strongly correlated to the numerical experiments reported here, and to describe the competition between several patterns and regimes.

4. Three numerical spectral codes

4.1. *The first code for no-slip boundary conditions (SST)*

The first code (SST), used in the present experiments, was written by P. Sulem, C. Sulem, and O. Thual and is described in Sulem *et al.* (1985). It has been run for the case of no-slip boundary conditions in a study of low-Prandtl-number convection (Meneguzzi *et al.* 1987). The so-called 'Kleiser–Schuman method' is used to eliminate the pressure by imposing the artificial boundary condition $\nabla \cdot \boldsymbol{v} = 0$ at the top and bottom. The resulting implicit linear equations coupling $\boldsymbol{v}$ and p are solved with the 'influence matrix method'. The boundary conditions $p = 1$ on a single collocation point of the plates, with $p = 0$ on the others, are successively imposed for the homogeneous linear equation. The solution of the complete linear equation with $p = 0$ imposed on all the collocation points of the plates is then solved. All these solutions are then combined in order to satisfy $\nabla \cdot \boldsymbol{v} = 0$ on the plates. This last boundary condition forces the system to relax to an incompressible field, but for inadequate resolution and too-large time steps the incompressibility can be too strongly violated.

The spatial scheme is pseudo-spectral, and the fields are expanded on Fourier series in the horizontal directions and Chebyshev polynomials in the vertical direction. The vertical boundary conditions are imposed through the 'Tau method'. The nonlinear terms are calculated on collocation points such that the mappings between the physical and spectral spare can be achieved through fast Fourier transforms. The temporal scheme is of second order, Adams–Bashforth for the nonlinear terms and the buoyancy terms and Crank–Nicolson for the other linear terms. The resolution of the Helmholtz and Laplace equations of this implicit scheme is done through the inversion of tridiagonal matrices, with a plain bottom line, after a suitable transformation.

The adaptation of SST to the zero-Prandtl-number equations (2.3) has been an easy task. The implicit treatment of the temperature evolution equation is just replaced by an implicit diagnostic equation. Four fast Fourier transforms are saved in this case.

On the Cray Y-MP, SST uses 0.051 s of CPU per time step, for the $x \times y \times z$ resolution $16^2 \times 32$, and 0.38 s of CPU for the $32^2 \times 64$ resolution. At zero Prandtl number a reduction of about 30% in these performances is achieved through the saving of fast Fourier transforms.

4.2. *The second code for no-slip boundary conditions (KER)*

The second numerical code for no-slip boundary conditions (KER) used for the present experiments has been written and is maintained by R. M. Kerr (see Wu, Lilly & Kerr 1991). It is based on a pseudo-spectral method developed by Moser, Moin & Leonard (1983) in which the basis functions for the velocity satisfy both the incompressibility constraint, the periodicity in two directions (through a Fourier decomposition), and the no-slip boundary conditions in a third direction.

The choice of the basis functions follows a poloidal–toroidal decomposition of the velocity-field analogue to (2.7), in which the unit vector $\boldsymbol{e}_3$, i.e. the direction of the projection, is replaced by one of the horizontal unit vectors, here the unit vector $\boldsymbol{e}_2$ in the y-direction. The projection of the Navier–Stokes (or Oberbeck–Boussinesq) equations onto a set of ordinary differential equations is accomplished by using a weighted residual method. The weight vectors chosen are such that the pressure term is eliminated and they yield matrices which are banded with small bandwidths in the implementation of the implicit temporal schemes. Quasi-orthogonal functions built with Chebyshev polynomials are used in the vertical directions, allowing the use of fast Fourier transforms for the evaluation of the nonlinear terms in the physical space.

In KER, a third-order Runge–Kutta time differencing is used for nonlinear and buoyancy terms while the Crank–Nicholson semi-implicit scheme is used for the viscous terms. A particularly convenient feature is the possibility of an adjustable time step base on the CFL criterion (taken equal to 2.5 here).

The adaptation of the KER code to the simulation of the $P = 0$ asymptotic equations (2.3) has been implemented by its author. The comparison between the results of KER and SST is a good test of the implementation of this feature in both codes.

The figures of 0.16 s of CPU per time step on the Cray Y-MP for the resolution $16^2 \times 32$ and 0.68 of CPU at the resolution $32^2 \times 64$ are obtained when running KER at finite Prandtl number.

4.3. *The code for free-slip boundary conditions (THU)*

For the purpose of this work, a pseudo-spectral code (THU) which allows free-slip boundary conditions has been written. These boundary conditions are obtained by imposing parity symmetries in the vertical direction to the various fields. For instance, the temperature deviation θ is even, choosing $z = 0$ at the bottom plate. These symmetries allow the use of cosine and sine transforms in the vertical directions. In the horizontal directions a Fourier decomposition is used.

Instead of eliminating the pressure by using the projection tensor $P_{ij}(\boldsymbol{k})$ on the solenoidal fields, as in Meneguzzi *et al.* (1987), the poloidal–toroidal decomposition described in §2 is used for the THU code. The temporal scheme is a 'slaved-frog' scheme, as described in Frisch, She & Thual (1986), to allow large time steps. In this scheme, a set of equations, $X_t = \mathrm{L}X + F$, where L is a linear operator and F contains the nonlinear terms, is discretized by

$$X^{(n+1)} = \mathrm{e}^{2\mathrm{L}\delta t} X^{(n-1)} + \mathrm{L}^{-1}(\mathrm{e}^{2\mathrm{L}\delta t} - 1)\, F^{(n)}. \tag{4.1}$$

When applied to (2.7), the linear operator L is chosen to match the terms on the right-hand side. This operator is block diagonal in the spectral space, the coupling between w and θ involving 2×2 matrices. The exponential of such matrices is calculated by the series $\sum_{n=0}^{N} \mathrm{L}^n / n!$, where N is such that the next term in the series

R/R_c	Veronis (1966)	Moore & Weiss (1973)	THU1	THU2	THU3	Nusselt
1.1	1.16	1.18	1.185	—	—	1.18
1.2	1.32	1.34	1.344	—	—	1.34
1.4	1.68	1.61	1.606	—	—	1.61
2	2.12	2.14	2.142	—	—	2.14
3	2.65	2.68	2.678	—	—	2.68
4	3.01	3.04	3.040	3.040	—	3.04
6	3.52	3.55	3.553	3.553	—	3.55
10	4.19	4.24	4.247	4.244	—	4.24
15	4.78	4.85	4.867	4.853	4.853	4.85
20	5.24	5.33	5.363	5.333	5.333	5.33
30	5.97	6.08	6.173	6.105	6.105	6.10
40	6.56	6.68	6.848	7.742	6.740	6.74
50	7.05	7.16	7.441	7.298	7.295	7.29
60	—	—	—	7.796	7.790	7.79
70	—	—	—	oscil.	oscil.	oscil.

TABLE 1. Test of the code THU for 2D simulations for free-slip boundary conditions, $P = 6.8$ and $k_x = k_c$. The three resolutions 16^2 (THU1), 32^2 (THU2), and 64^3 (THU3) are compared to the literature.

must be smaller than a specified threshold. Numerical problems occur when this method is applied without care to matrices containing large numbers. For such matrices, $\exp(\mathrm{L}/M)$ is first calculated with the series, where M is an integer of the order of the norm of L, and the Mth power of the matrix obtained is computed to obtain the desired matrix $\exp \mathrm{L}$. With this procedure, the terms of the series are always of order 1, and there is no longer a numerical problem.

The advantage of this 'slaved-frog' temporal scheme is the ability to handle stiff problems, as is the case here for low-Prandtl-number convection where the diffusive and thermal times are very different. However, it must be noticed that for this scheme, the nonlinear terms F do not conserve energy. It seems, however, that the artificial dissipation of the scheme is negligible for the regimes studied here.

A first 2D test of this code has been performed by comparing it with various results in the literature (Veronis 1966; Moore & Weiss 1973). Table 1 lists the Nusselt numbers of 2D rolls of this comparison for the test value $P = 6.8$. A perfect agreement is obtained until the onset of the 2D oscillations. The experiments presented below, in §5, provide a satisfactory test of this new code when compared to the results of Meneguzzi *et al.* (1987), obtained with a different code and using a different spectral method.

With the resolution 16^3 the THU code takes 0.062 s of CPU for finite Prandtl number and 0.039 s of CPU for zero Prandtl number, per time step on the Cray Y-MP.

5. No-slip boundary conditions

5.1. *Stable travelling waves and the oscillatory instability*

These numerical experiments start with an investigation of the prediction by Fauve *et al.* of subcritical oscillatory instability for small Prandtl numbers and values of the aspect ratio k_x smaller than a specified threshold (e.g. $k_x < 2.9$ for $P = 0.025$ and $k_y = 2.2$). Both cases, $P = 0$ and $P = 0.025$, are considered, and the four values

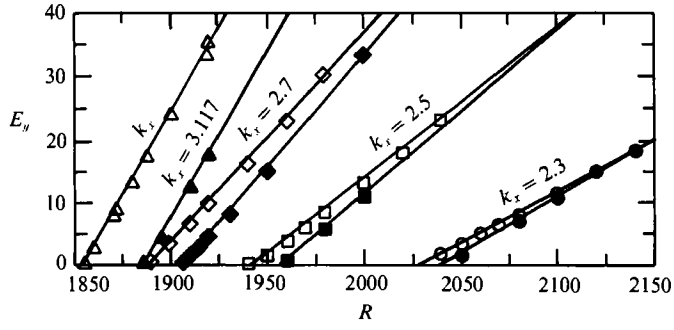

FIGURE 1. Bifurcation diagram of the oscillatory instability for $P = 0$ (open symbols) and $P = 0.025$ (filled symbols), and for $k_x = 3.177$, 2.7, 2.5 and 2.3. The value of $k_y = 2.2$ is fixed.

R	$E_{w\theta}$	E_y	Regime	Code
1855	39.4	0.17	TW	SST1
1860	39.1	3.1	TW	SST1
1870	39.4	8.2	TW	SST1
1872	40.1	9.2	TW	KER1
1880	39.7	13.5	TW	SST1
1888	40.7	17.7	TW	KER1
1900	40.3	24.3	TW	SST1
1920	41.0	35.5	TW	SST1
1920	41.7	34.8	TW	KER1
2000	45.8	77	TW	KER1
2050	49.3	106	TW	KER1
2080	51.6	125	TW	KER1
2100	53.4	140	TW	KER1
2100	52.5	166	TW	SST1
2140	57.3	168	TW	KER1
2160	59.4–59.7	182–188	MW	KER1
2192	63.1–63.2	208–212	MW	KER1
2200	63.7–64.6	208–228	MW	KER1
2200	62.5–63.0	267–278	MW	SST1
2220	64.3–64.9	216–224	MW	KER1
2220	63.5–64.0	270–292	MW	SST1
2240	68.4–69.6	240–272	unst ? MW	KER1
2240	66–73	250–420	unst ? MW	SST1

TABLE 2. Travelling waves (TW) for no-slip boundary conditions, $P = 0$, $k_x = 3.117$ and $k_y = 2.2$. The resolution $16^2 \times 32$ has been used for the two codes (SST1 and KER1). Modulated wave regimes are also listed.

$k_x = 3.117$, 2.7, 2.5 and 2.3 are explored, with $k_y = 2.2$ fixed. Figure 1 shows the corresponding bifurcation diagram where $E_y = \langle v^2 \rangle^{xyz}$ is plotted as a function of R. In all cases the oscillatory instability is supercritical and leads to stable travelling waves. Numerical values of $E_{w\theta} = \langle w\theta \rangle^{xyz}$ and E_y are listed in table 2 ($P = 0$) and table 3 ($P = 0.025$) for the particular case $k_x = 3.117$. Most of these bifurcation diagrams have been calculated with the SST code, but some comparisons with the KER code show good agreement.

Other values of k_y have been explored, leading to the same result. The most unstable wavenumber k_y is known to be 2.2 for $P = 0.025$ and $k_x = 3.117$ (Fauve *et al.* 1987). A numerical exploration shows that $k_y = 1.9$ is close to the most unstable wavenumber for $P = 0$, $k_x = 2.7$, as shown by the maximum of the travelling-wave

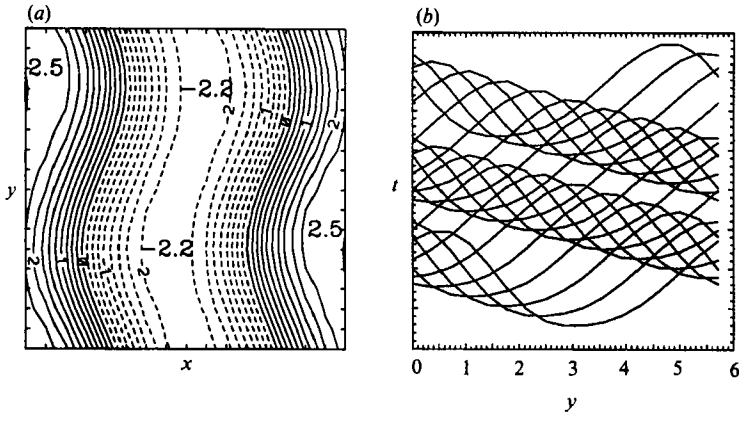

FIGURE 2. Travelling wave regime for no-slip boundary conditions, $P = 0$, $R = 1920$, $k_x = 3.117$ and $k_y = 2.2$. (*a*) Horizontal contours of θ at $z_0 = \frac{1}{2}$. (*b*) Time evolution of a y-profile of θ at $x_0 = \pi/k_x$ and $z_0 = \frac{1}{2}$.

R	E_{w0}	E_y	Regime	Code
1886	39.8	0.078	TW	SST1
1888	40.1	0.77	TW	SST1
1895	40.3	4.4	TW	SST1
1900	40.5	5.0	TW	SST1
1910	40.8	12.4	TW	SST1
1920	41.0	17.8	TW	SST1
1930	41.3	22.4	TW	SST1
2000	43.0	61	TW	KER2
2000	44.0	65	TW	SST1
2100	49.9	135	TW	SST1
2200	58.1	224	TW	SST1
2250	63.0	275	TW	SST1
2260	63.9–64.0	285–287	MW	SST1
2270	64.9–65.1	296–300.5	unst. MW	SST1
4000	268–320	2340–3460	chaotic MW	KER2

TABLE 3. Travelling waves (TW) for no-slip boundary conditions, $P = 0.025$, $k_x = 3.117$ and $k_y = 2.2$. The resolutions $16^2 \times 32$ (SST1) and $32^2 \times 64$ (KER2) have been used. Modulated wave regimes (MW) are also listed.

amplitude at $R = 1920$ (which is a Rayleigh number close to the onset of the oscillatory instability). There is little chance of finding subcritical behaviour, even if one cannot rule it out completely. The theoretical approach for no-slip boundary conditions proposed by Fauve *et al.* (1987) must be revisited by including, for instance, more nonlinear terms in their model.

An example of these travelling waves for $P = 0$ shown in figure 2. The same features are observed for small but finite Prandtl numbers. A sinusoidal deformation of the roll in their axis direction y propagates at a constant speed along the axis. This deformation is symmetric with respect to this reflection $y \rightarrow -y$. The propagation speed is non-zero at the onset of the oscillatory instability. The mean shear $V(z)$ has a sinusoidal form and is stationary while $U(z)$ is zero. Its amplitude of V grows quadratically with the distance $R - R_{\mathrm{II}}$, as can be seen from (2.2), and as observed by Clever & Busse (1989) for finite Prandtl numbers.

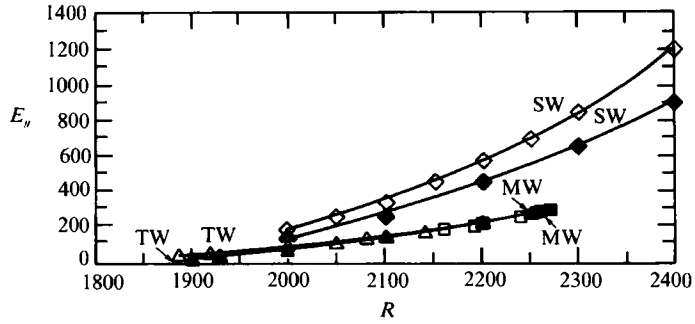

FIGURE 3. Bifurcation diagram of the travelling waves (TW) and standing waves (SW) competition, for no-slip boundary conditions, $P = 0$ (open symbols) and $P = 0.025$ (filled symbols), with $k_x = 3.117$ and $k_y = 2.2$.

R	E_{w0}	E_y	Regime	Code
1920	42–64	68.8	unst. SW	KER1
1950	44–50	104	unst. SW	KER1
2000	46–55	170	unst. SW	SST2
2000	47–55	152	unst. SW	KER1
2050	50–64	252	unst. SW	SST2
2080	missing	264	unst. SW	KER1
2100	56–74	342	unst. SW	SST2
2140	62–84.5	432	unst. SW	KER1
2150	62–85	450	SW	SST2
2160	65–89	482	SW	KER1
2200	68–96	570	SW	SST2
2240	78–112	692	SW	KER1
2250	79–114	700	SW	SST2
2260	82–119	744	SW	KER1
2288	missing	816	SW	KER1
2300	89–131	850	SW	SST2
2320	97–140	928	SW	KER1
2350	99–149	1040	SW	SST1
2400	110–170	1200	SW	SST1
2400	110–170	1200	SW	SST2
2400	missing	1216	SW	KER1
2480	134–208	1528	SW	KER1
2500	100–218	1620	SW	SST2
2560	161–252	1888	SW	KER1
2600	169–267	128–2040	SW	KER1
3000	375–580	600–5100	SW	SST2

TABLE 4. Standing waves (SW) for no-slip boundary conditions, $P = 0$, $k_x = 3.117$ and $k_y = 2.2$. The resolutions $16^2 \times 32$ (KER1) and $32^2 \times 64$ (SST2) have been used.

The present values of R_{II} compare well with the values calculated by Clever & Busse (1974, 1989, 1990), using a stability analysis. The contribution of this section consists in a wider exploration of the aspect ratios k_x and k_y to rule out the prediction of Fauve *et al.* (1987).

5.2. *Competition between travelling waves and standing waves*

The study of the next instabilities, for the two cases $P = 0$ and $P = 0.025$, is now restricted to the aspect ratios $k_x = 3.117$ and $k_y = 2.2$. Figure 3 displays the experimental bifurcation diagram of the oscillatory instability, where the two

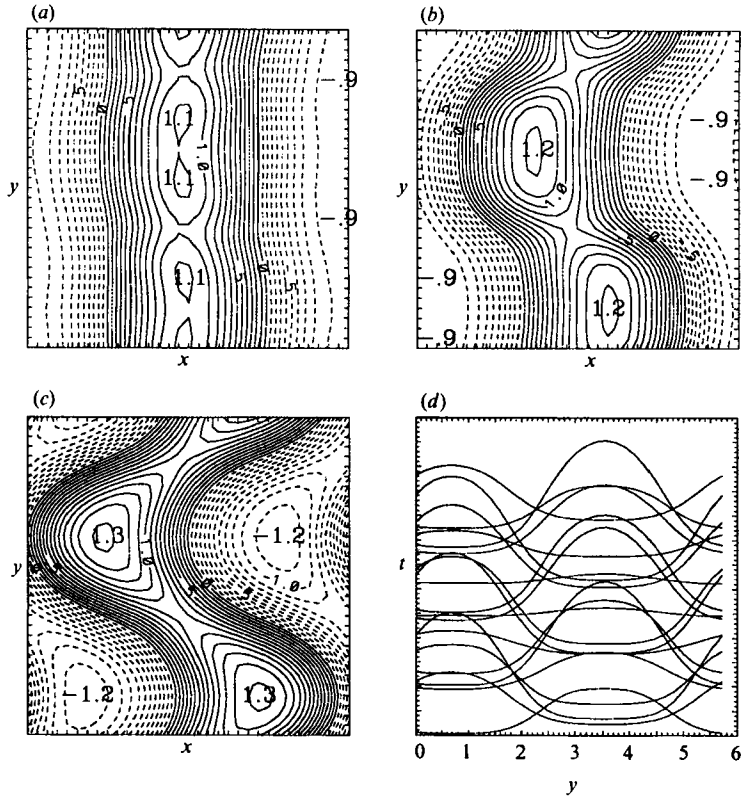

FIGURE 4. Standing wave regime for no-slip boundary conditions, $P = 0$, $R = 2400$, $k_x = 3.117$ and $k_y = 2.2$. (*a*)–(*c*) Horizontal contours of θ at $z_0 = \frac{1}{2}$ and different times. (*d*) Time evolution of a y-profile of θ at $x_0 = \pi/k_x$ and $z_0 = \frac{1}{2}$.

R	$E_{w\theta}$	E_y	Regime
1900	40.8–41.3	12	unst ? SW
2000	44.8–51.2	124	SW
2100	52.8–65.6	250	SW
2200	62.4–83.2	450	SW
2300	76.8–106	650	SW
2400	91.2–130	900	SW
2500	109–157	1150	SW
2600	126–186	1450	SW
2700	146–216	1780	SW

TABLE 5. Standing waves (SW) for no-slip boundary conditions, $P = 0.025$, $k_x = 3.117$ and $k_y = 2.2$. The resolution $32^2 \times 64$ (SST2) has been used.

Prandtl-number cases have been superimposed. Table 4 ($P = 0$) and table 5 ($P = 0.025$) give the corresponding values of $E_{w\theta}$ and E_y, and provide a satisfactory comparison between two resolutions and the two no-slip boundary-condition codes.

When the Rayleigh number is increased, the stable travelling wave regime described in the previous section is destabilized at $R = R_{\mathrm{III}}$ through a secondary oscillatory instability, i.e. a Hopf bifurcation of the Poincaré mapping. With the appearance of a second frequency, incommensurable with the primary travelling wave frequency, the trajectories in the phase space lie on a torus. This regime is

called 'modulated waves' in the classification of Crawford & Knobloch (1991) for the secondary bifurcations of an oscillatory instability with $O(2)$ symmetry. Based on the present numerical experiments, it is hard to decide whether this bifurcation is supercritical or subcritical. Indeed, very long transients, eventually leading to a standing wave regime, are observed for values of R only slightly greater than R_{III}. Other runs, at R very close to R_{III}, could not be integrated long enough to decide whether their observed modulated wave behaviour was transient or not. If not, the interval $[R_{\mathrm{III}}, R_{\mathrm{SW}}]$ of stability of this regime is very small, and ends with a saddle-node bifurcation at R_{SW}, which leads to a stable standing wave regime.

These results cannot be compared directly with Clever & Busse (1987, 1989, 1990) who investigated different values of the aspect ratios k_x and k_y. In both cases they observe a stable modulated wave regime on a large interval of the Rayleigh number past the bifurcation values R_{III}. Their results compare well with the numerical experiments of Lipps (1976) and McLaughlin & Orszag (1982). But it should be checked whether these modulated wave regimes are very long transients, or part of some intermittent regimes with very long laminarization periods. This hypothesis would be consistent with the long run performed in the present experiment (but not shown here) for $P = 0.025$ and $R = 4000$; after staying on an intermittent regime for a very long time, the system seems to relax to a modulated wave regime which is, in fact, weakly chaotic.

Standing waves are stable up to high values of the Rayleigh number. For this regime the maximum of E_y has been displayed in figure 3. Figure 4 shows a standing wave regime. A null mean shear $U(z)$ characterizes these states, in accordance with their symmetries. These stable standing waves are competing with the stable travelling waves, i.e. they are stable on a common interval of the control parameter, starting at a Rayleigh number R_{MW}. (This value has to be greater than R_{II} as predicted by instability theory.) The numerical determination of R_{MW} is difficult because it has a long transient. Metastable standing wave regimes are indeed observed between R_{II} and R_{MW}. For R close to R_{II}, these transients are much longer, as would be predicted by linear arguments. When starting with random conditions of 2D rolls perturbed by a spatial white noise, standing wave regimes seem to be selected at first. This suggests the following picture: a stable manifold drags many initial conditions to the vicinity of the unstable standing wave regimes, while a weak and slow unstable manifold eventually connects the trajectories to the stable travelling wave regime.

5.3. *Intermittence and pattern competition*

When the Rayleigh number is further increased, the standing waves become unstable, and a scenario of transition to chaos takes place. This scenario is not investigated in detail here, and it cannot be decided whether the avenue to chaos is a period-doubling transition to a strange attractor, the appearance of two other frequencies, some kind of intermittence, or another picture.

After this transition, an intermittent regime eventually occurs. The time series of this regime, for $E_{w\theta}$ and E_y, are displayed in figure 5 for $P = 0$ and $R = 4000$. This figure also provides a qualitative comparison between the SST code and the KER code; different initial conditions have been used for the two simulations, and after the transients, not shown of the figure, the regimes obtained with the two codes are qualitatively identical.

The nature of this intermittent regime can be understood from the contour plots of figure 6. During the quiescent periods, the flow is in a 2D roll pattern. A small and

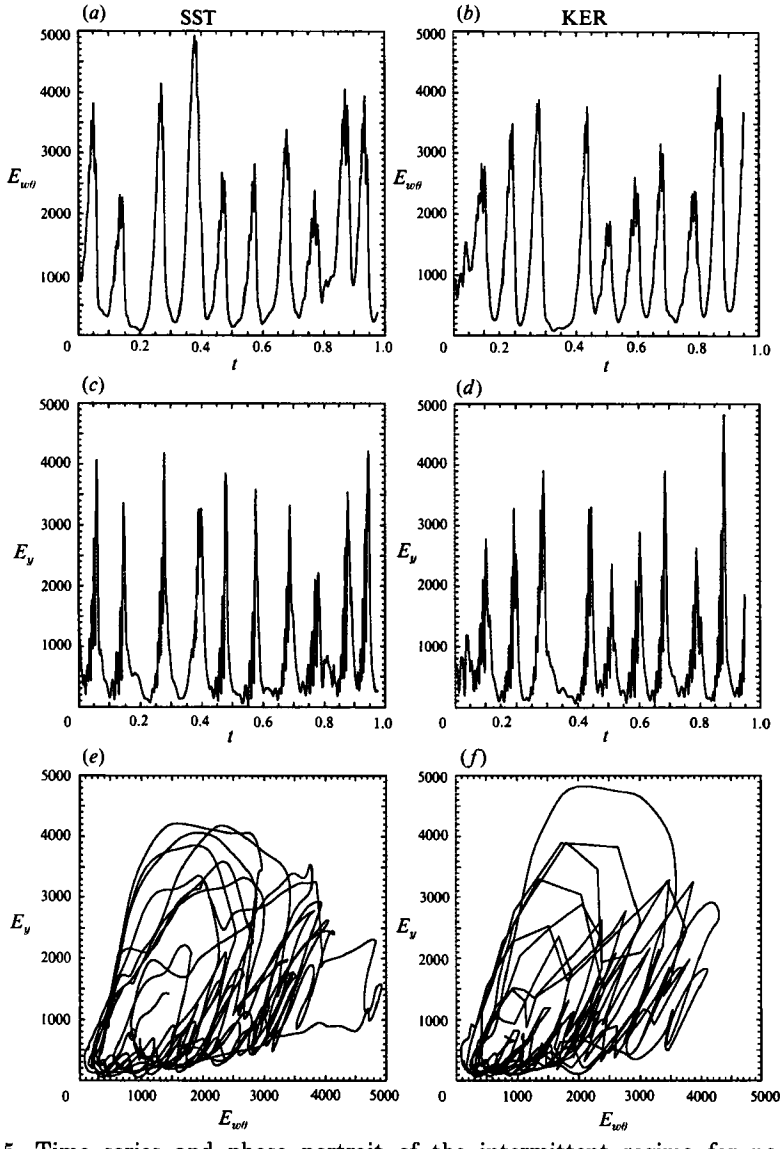

FIGURE 5. Time series and phase portrait of the intermittent regime for no-slip boundary conditions, $P = 0$, $R = 8000$, $k_x = 3.117$ and $k_y = 2.2$ and a qualitative comparison between the codes SST (left-hand panels) and KER (right-hand panels) at the resolution $32^2 \times 64$. The initial conditions for the two codes are not the same, and the transients are not shown here. (*a*), (*b*) Time evolutions of E_{w0}. (*c*), (*d*) Time evolutions of E_y. (*e*), (*f*) Phase portraits E_{w0} versus E_y.

growing oscillation, with a standing wave pattern, eventually reaches very high amplitude. The convection rolls are bent to the degree that they break into cellular patterns with a polygonal shape. The intensity of the convection in these cells then decreases to a level where 2D rolls are observed again. This behaviour suggests the presence of a homoclinic orbit for the 2D rolls' stationary state. The unstable manifold is associated with the oscillatory instability, and the stable manifold is a result of the competition between the 2D rolls and other possible polygonal patterns, such as hexagons or squares.

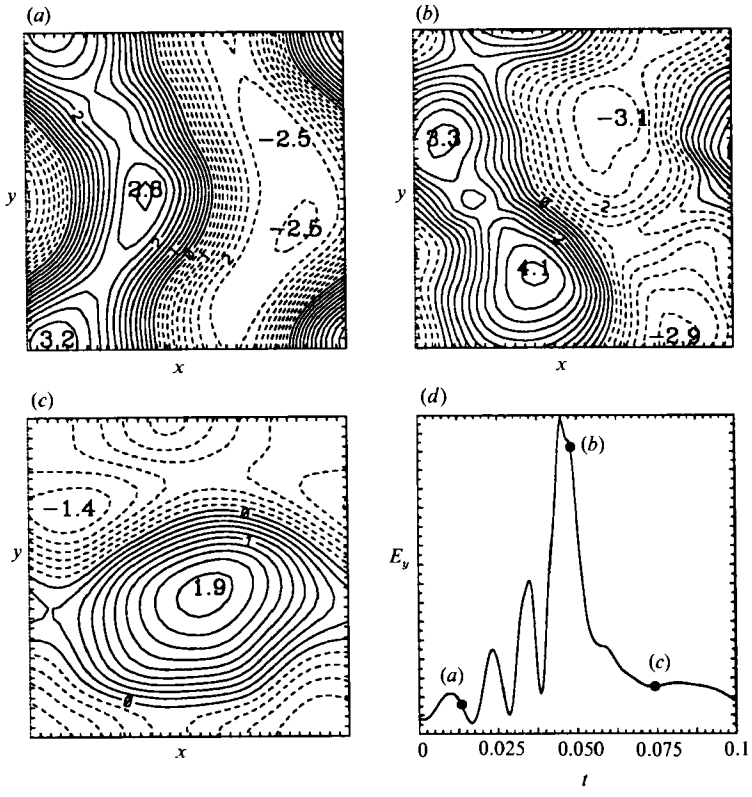

FIGURE 6. Pattern competition in the intermittent regime for no-slip boundary conditions, $P = 0$, $R = 8000$, $k_x = 3.117$ and $k_y = 2.2$. (*a*)–(*c*) Horizontal contours of θ at $z_0 = \frac{1}{2}$ at $t = 0.0125, 0.05$ and 0.875 respectively. (*d*) Time evolution of E_y for $t \in [0, 0.1]$.

	R	$\log_{10} E_{w0}$	$\log_{10} E_y$	$\log_{10} E_{\text{tot}}$
(*a*)				
	4000	3.18	3.92	4.93
	8000	3.74	4.72	5.55
	16000	4.30	5.37	6.33
	32000	4.87	5.98	6.74
	64000	5.44	6.61	7.34
	128000	6.03	7.25	7.95
	256000	6.89	8.19	8.84
(*b*)				
	4000	2.49	3.48	4.33
	8000	2.78	4.12	4.78
	16000	2.91	4.70	5.04
	32000	3.16	5.10	5.44
	64000	3.34	5.43	5.77
	128000	3.50	5.78	6.11

TABLE 6. Chaotic regimes for no-slip boundary conditions, $k_x = 3.117$, $k_y = 2.2$ and (*a*) $P = 0$, (*b*) $P = 0.025$. The resolution $32^2 \times 64$ and the code KER has been used (KER2).

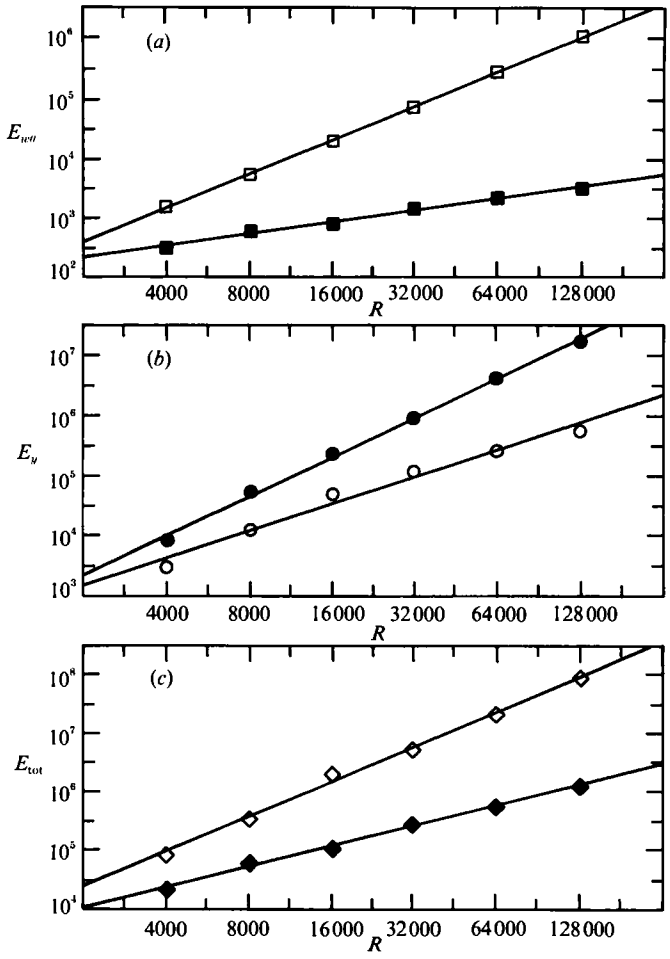

FIGURE 7. Scaling laws of (*a*) $E_{w\theta}$, (*β*) E_y, and (*c*) $E_{\rm tot}$ for no-slip boundary conditions, $P = 0$, (open symbols) and $P = 0.025$ (filled symbols).

5.4. *Scaling laws of the first Rayleigh-number decade*

Very long integrations for both $P = 0$ and $P = 0.025$ have been performed in order to investigate the first Rayleigh-number decade scaling laws of the time average $\langle E_{w\theta}\rangle^t = \langle w\theta\rangle^{xyzt}$, $\langle E_y\rangle = \langle v^2\rangle^{xyzt}$, and $\langle E_{\rm tot}\rangle = \langle \boldsymbol{v}^2\rangle^{xyzt}$. The values of these quantities, calculated for six Rayleigh numbers in geometric progression from $R = 4000$ *to* 128,000, are listed in table 6(*a*) ($P = 0$) and table 6(*b*) ($P = 0.025$), and displayed in figure 7. They are fitted by the scalings laws

$$\left.\begin{aligned}\langle E_{w\theta}\rangle^t &= 4.41\times10^{-3}(R-R_{\rm c})^{1.647},\\ \langle E_y\rangle^t &= 5.12\times10^{-3}(R-R_{\rm II})^{1.870},\\ \langle E_{\rm tot}\rangle^t &= 116\times10^{-3}(R-R_{\rm c})^{1.745}\end{aligned}\right\} \tag{5.1}$$

for $P = 0$, with $R_{\rm II} = 1855$, and

$$\left.\begin{aligned}\langle E_{w\theta}\rangle^t &= 3.37(R-R_{\rm c})^{0.584},\\ \langle E_y\rangle^t &= 0.156(R-R_{\rm II})^{1.292},\\ \langle E_{\rm tot}\rangle^t &= 7.53(R-R_{\rm c})^{1.029}\end{aligned}\right\} \tag{5.2}$$

for $P = 0.025$, with $R_{\rm II} = 1885$.

R	$E_{w\theta}$	E'_y	Regime
720	3.380	1.9	TW
740	3.379	3.18	TW
760	3.390	4.9	TW
780	3.410	6.74	TW
790	3.413	7.8	TW
800	3.441	8.55	TW
810	3.461	9.41	TW
820	3.483	10.385–10.388	MW

TABLE 7. Travelling waves (TW) for free-slip boundary conditions, $P = 0.02$ and $k_x = k_y = k_c$. The resolution 16^3 (THU1) has been used.

R	$E_{w\theta}$	E'_y	Regime
710	4.63–4.66	0.06–0.88	unst. SW
720	4.61–4.70	0.2–2.55	unst. SW
740	3.32–3.55	0.4–5.8	unst. SW
760	3.30–3.65	0.6–9	unst. SW
790	3.30–3.82	1–14	unst. SW
800	3.42–4.00	2.1–16.5	unst. SW
820	3.87–4.47	7–22	MW
830	4.05–4.75	9.3–25	MW
840	3.50–5.87	7–32	BW
850	3.20–6.75	7–87	BW
860	3.0–7.5	5–43	BW
870	3.0–8.0	5–48	BW
880	3.0–8.5	5–53	BW
900	3.0–9.7	5–62	BW
920	3.0–10.0	4–76	CW
950	3.5–10.5	5–105	CW
1000	3.5–12.5	5–760	IW
1000	6.37	128	SQ
1020	6.52	135	SQ

TABLE 8. Regime for free-slip boundary conditions, $P = 0.2$ and $k_x = k_y = k_c$: modulated waves (TW), biperiodic waves (BP), intermittent waves (IW), and chaotic waves (CW). The resolution 16^3 (THU1) has been used.

The slope of $\langle E_{w\theta} \rangle^t$ for $P = 0.025$ is the same as the slope that would be obtained for the Nusselt number, and it is higher than the experimental, numerical, or theoretical values (see Busse 1981) found in the literature for high Rayleigh numbers. But it must be remembered that only the first decade and a half of the Rayleigh number is investigated here. For these low values of R, only the comparison between finite and zero Prandtl numbers is of any interest. All the slopes are much higher at zero Prandtl numbers, which suggests that the scaling at small Prandtl numbers differs from the order-one Prandtl convection. This is probably because thermal boundary layers completely disappear at zero Prandtl number.

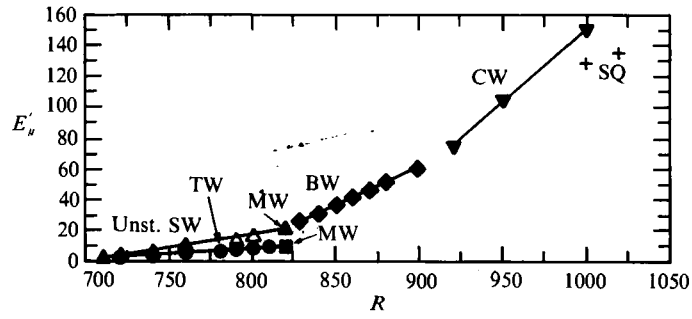

FIGURE 8. Bifurcation diagram for free-slip boundary conditions, $P = 0.2$ and $k_x = k_y = k_c$. Regimes: travelling waves (TW), standing waves (SW), modulated waves (MW), biperiodic waves (BP), chaotic waves (CW), intermittent waves (IW), and stationary squares (SQ).

R	$E_{w\theta}$	E'_y	Regime	Code
700	2–30	0–900	SQOR	THU2
800	7.5	110	SQ	THU2
880	missing	144.4	SQ	THU1
900	8	150	SQ	THU2
1000	29	450–505	HXOS	THU2
1000	29.3	457–511	HXOS	THU1
1020	32	490–558	HXOS	THU2
1020	44–56	450–1350	SQCH	THU1
1040	35	530–610	HXOS	THU2
1040	42–66	400–1500	SQCH	THU1
1060	35–70	300–1700	SQCH	THU1
1100	50–51	720–980	HXOS	THU2
1100	35–100	400–2200	SQCH	THU1
1200	40–100	600–1800	HXCH	THU2
1200	60–180	1000–4500	SQCH	THU1
1300	30–130	600–2300	HXCH	THU2
1300	40–100	500–4500	SQCH	THU1
1500	40–105	800–2300	HXCH	THU2
1600	60–220	1000–4000	HXCH	THU2
1700	110–155	1600–4400	HXCH	THU2

TABLE 9. Regimes for free-slip boundary conditions, $P = 0$ and $k_x = k_y = k_c$: stationary squares (SQ), intermittent oscillations of squares (SQOR), oscillations of hexagons (SQOS), and chaotic regimes (SQCH and HXCH). The resolutions 16^3 (THU1) and 32^2 (THU2) have been used.

6. Free-slip boundary conditions

6.1. *Transition to chaos for a finite Prandtl number* ($P = 0.2$)

The first numerical experiments for free-slip boundary conditions, using the code THU, reproduce and complete the experiments performed for $P = 0.2$ and $k_x = k_y = k_c = \pi/\sqrt{2}$ in Meneguzzi *et al.* (1987), with a different code, as described in §4. Numerical values of $E_{w\theta} = \langle w\theta \rangle^{xyz}$ and $E'_y = \langle (v-V)^2 \rangle^{xyz}$ are listed in table 7 and table 8. The corresponding bifurcation diagram showing E'_y as a function of R is shown in figure 8. These values are in agreement with Meneguzzi *et al.* (1987) and complete the understanding of the transition to chaos.

The competition between travelling waves and standing waves near the onset of the oscillatory instability leads to a bifurcation diagram similar to the one observed with no-slip boundary conditions. Travelling waves bifurcated supercritically at

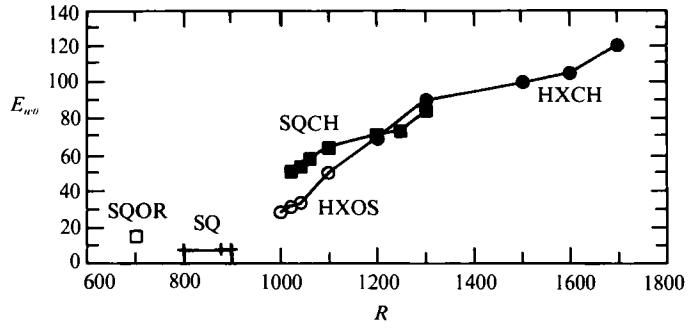

FIGURE 9. Partial bifurcation diagram for free-slip boundary conditions, $P = 0$ and $k_x = k_y = k_c$. Regimes: stationary squares (SQ), relaxation oscillating squares (SQOR), oscillating squares (SQOS), chaotic squares (SQCH), oscillating hexagons (HXOS), and chaotic hexagons (HXCH).

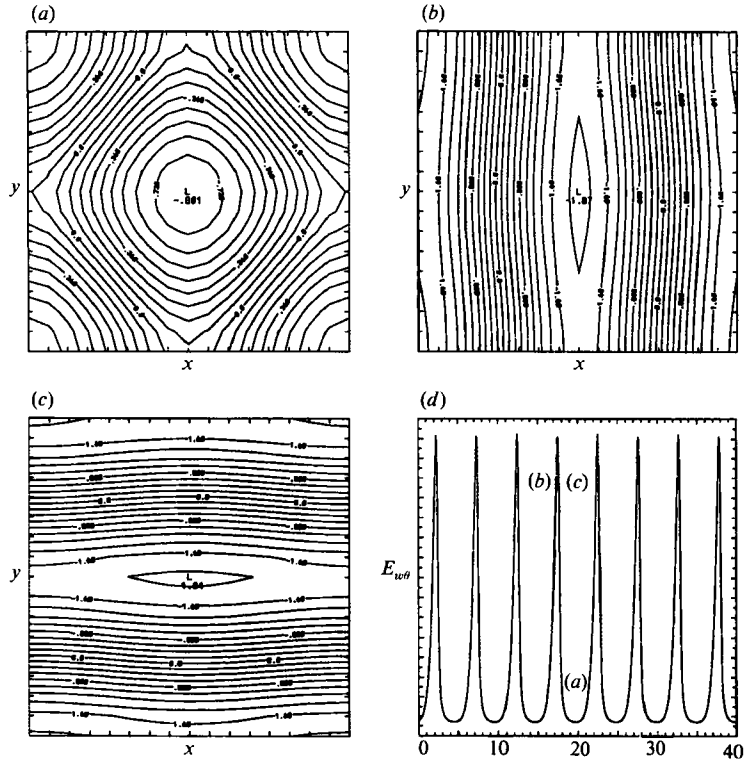

FIGURE 10. Relaxation oscillation regime (SQOR) with basic square pattern for free-slip boundary conditions, $P = 0$, $R = 700$ and $k_x = k_y = k_c$. (*a*) Horizontal contours of θ at $z_0 = \frac{1}{2}$ during the quiescent periods. (*b*), (*c*) The same contours during the next burst. (*d*) Time evolution of $E_{w\theta}$.

$R = R_{II}$. At $R = R_{III}$ the appearance of a new frequency leads to a modulated wave regime. This transition is likely to be subcritical or closely followed by a saddle-node bifurcation, as indicated by the long transients observed near R_{III}. These transients of modulated waves, which can be interpreted as a main travelling wave mixed with a small-amplitude, counterpropagating wave, eventually jump abruptly to another type of modulated wave made of two counterpropagating waves of equivalent but not exactly equal amplitudes. This upper branch of modulated waves computes with the travelling wave regime down to a value $R = R_{MW}$, which is hard to determine numerically. Unstable standing waves are also observed between R_{II} and R_{MW}

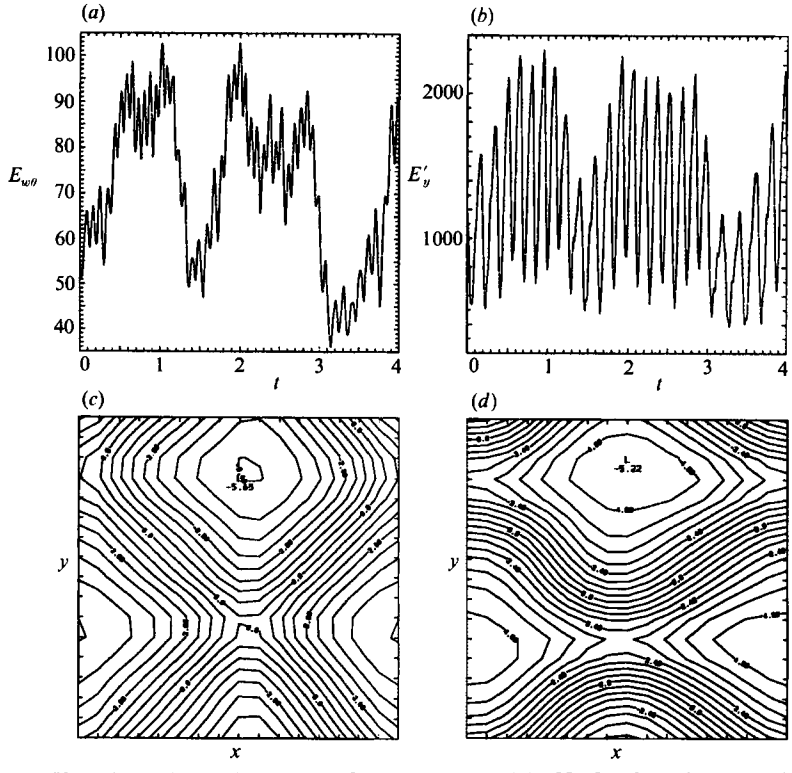

FIGURE 11. Chaotic regime with square basic pattern (SQCH) for free-slip boundary conditions, $P = 0$, $R = 1100$ and $k_x = k_y = k_c$. (*a*), (*b*) Time evolution of E_{w0} and E'_y. (*c*), (*d*) Horizontal contours of θ at $z_0 = \frac{1}{2}$ at different times.

through long transients, as for the case of no-slip boundary conditions. The detailed bifurcation diagram which explains this behaviour is not investigated here. But such complicated connections between travelling waves, standing waves and modulated waves are not surprising, as can be seen from the classifications of Golubitsky *et al.* (1988).

The upper-branch modulated waves encounter a transition to chaos when the Rayleigh number is further increased. This transition is probably achieved through a period-doubling cascade, as suggested by the observation of biperiod regimes and eventually chaotic regimes followed by intermittent regimes. The precise nature of this scenario is not investigated here. Further information about this transition to chaos can be found in Busse & Sieber (1991).

In competition with these chaotic regimes, a stationary square pattern has been observed at around $R = 1000$. The continuation of this branch down to the onset of convection, and up to a transition to chaos, is not undertaken in the present experiments. Multiple and complex regimes are expected from such a study, which would require extended computer resources. However, this stationary regime can be connected to the zero-Prandtl-number case, as shown in §6.3.

6.2. *Regimes for zero Prandtl number*

The next experiments, performed with the code THU, are the first exploration of the case $P = 0$, for the same values $k_x = k_y = k_c$ as above. Numerical values associated with these experiments are listed in table 9 and represented in the partial bifurcation diagram of figure 9. More regimes should be observed by a complete exploration, but

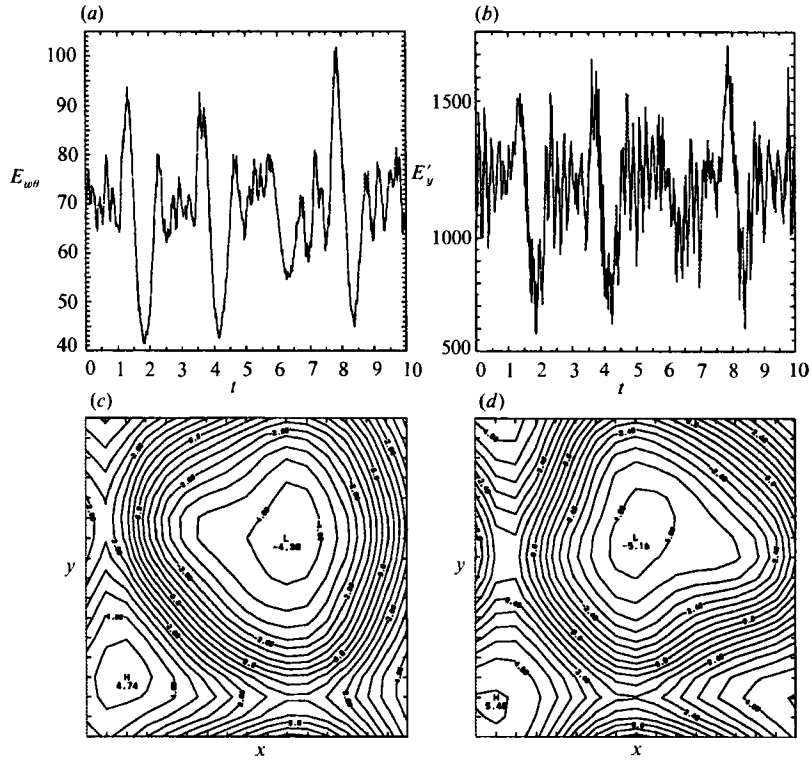

FIGURE 12. Chaotic regime with hexagonal basic pattern (HXCH) for free-slip boundary conditions, $P = 0$, $R = 1200$ and $k_x = k_y = k_c$. (*a*), (*b*) Time evolution of $E_{w\theta}$ and E'_y. (*c*), (*d*) Horizontal contours of θ at $z_0 = \frac{1}{2}$ at different times.

the purpose of this Section is only to illustrate the variety of these regimes for a few examples.

Starting with initial conditions exactly equal to a linearly unstable 2D mode would lead the system to infinity, as explained in §3. A small random perturbation is added to such an initial condition to see if a system would eventually reach a bounded attractor. Numerical simulations performed by Herring (1970) suggested that even a random perturbation of this initial condition would lead to blow-up behaviour.

An investigation of this prediction is performed here for $R = 700$, with a white noise perturbation of a 2D roll as initial condition. Contrary to what was expected, the system eventually reaches a bounded attractor. The initial exponential growth of the initiated 2D roll is indeed interrupted by the competition with the orthogonal 2D mode, seeded by the random perturbation. The asymptotic regime attained in this experiment consists in relaxation oscillations with a square pattern, whose characteristics are displayed in figure 10. During a long period of time the two orthogonal modes have the same amplitude, and a perfectly square pattern is observed. But this long stationary period is followed by a burst of one of the modes and relaxation to the quasi-equilibrium state. The same burst occurs for the other mode, after waiting an equal amount of quasi-stationary time; this alternance repeats itself periodically. In other words, there exists a periodic orbit which spends a long time near a stationary square pattern.

For higher Rayleigh number, stable stationary squares are observed. The connection between these square regimes and those of relaxation oscillations with a

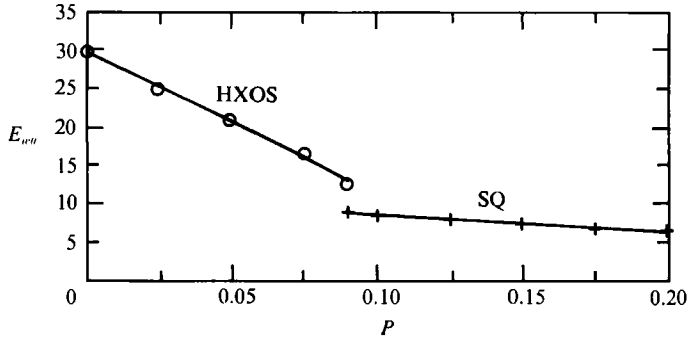

FIGURE 13. Variation of $\epsilon[0, 0.2]$ for free-slip boundary conditions, $R = 1000$ and $k_x = k_y = k_c$. Regimes: stationary squares (SQ) and oscillating hexagons (HXOS).

P	E_{w0}	E'_y	Regime
0	29.8	457–510	HXOS
0.025	24.9	384–434	HXOS
0.050	21.0	331–372	HXOS
0.075	16.7	272–303	HXOS
0.090	12.7	220–240	HXOS
0.090	8.79	183	SQ
0.100	8.57	178	SQ
0.125	7.96	165	SQ
0.150	7.42	152	SQ
0.175	6.86	139	SQ
0.200	6.37	128	SQ

TABLE 10. Variation of $P \epsilon [0, 0.2]$ for $R = 1000$ and $k_x = k_y = k_c$: stationary squares (SQ) and oscillating hexagons (HXOS). The resolution 16^3 (THU1) has been used.

square pattern, likely to be described by a global bifurcation approach, is not investigated here. For higher Rayleigh number two kinds of patterns are observed. oscillating and chaotic regimes with a square basic pattern (figure 11) are observed in competition with oscillating and chaotic regimes with a quasi-hexagonal basic pattern (figure 12)

6.3. *From small to zero Prandtl numbers*

In order to make a connection between finite- and zero-Prandtl-numbers regimes, the stationary square regime, obtained for $P = 0.2$ and $R = 1000$, has been used as a starting point for a numerical experiment where the Prandtl number is decreased continuously from $P = 0.2$ to $P = 0$. The numerical values corresponding to this experiment are listed in table 10, and the corresponding bifurcation diagram is displayed in figure 13. The stationary square pattern, stable at $P = 0.2$, seems to undergo a subcritical bifurcation around $P = 0.08$; but the accurate establishment of this statement is not important here. Past this instability the system jumps to hexagonal oscillations which are continuously connected to the identical regimes observed at $P = 0$. This experiment shows that even for free-slip boundary conditions, the zero-Prandtl-number equations are a proper limit for small-Prandtl-numbers regimes.

7. Conclusion

The zero-Prandtl-number, Oberbeck–Boussinesq equations have been numerically simulated for both no-slip boundary conditions and free-slip boundary conditions in a small-aspect-ratio geometry. The derivation of these equations assumes an asymptotic behaviour of the solutions which is consistent with the numerical experiments performed at low Prandtl number.

For no-slip boundary conditions, the bifurcation diagrams of the first instabilities for $P = 0$ and $P = 0.025$ are very close. The oscillatory instability is supercritical for a large class of aspect ratios, and leads to stable travelling waves. The observed secondary instabilities, resulting from the competition with the standing waves is consistent with amplitude-equation predictions, based on degeneracy studies. Instead of documenting the precise scenario of the transition to chaos encountered by these standing waves, the focus has been on the competition between patterns. An intermittent regime, involving standing waves and a polygonal pattern, is observed at high Rayleigh numbers. Scaling laws for E_y, E_{tot} and $E_{w\theta}$, in the first decade of variation of R above the oscillatory instability, show an important, but finite, increase in the slope at zero Prandtl number. These experiments have been performed with two different codes (SST and KER) in perfect agreement.

For free-slip boundary conditions, the bifurcation diagram obtained for $P = 0.2$ is very similar to the case of no-slip boundary conditions. The competition between travelling waves and standing waves eventually leads to modulated waves, which encounter a transition to chaos. However, this bifurcation diagram is not appropriate in the limit $P \to 0$, because the stationary 2D roll patterns are pushed to infinity. Instead, other patterns such as squares or hexagons are selected, and they undergo various instabilities, e.g. the oscillatory instability, and eventually a transition to turbulence. These zero-Prandtl-number patterns are continuously connected to finite-Prandtl-number regimes.

These numerical simulations open a new field of applications for instability studies and are characterized by the fact that the stationary and oscillatory instabilities are interacting closely, and even exactly at $P = 0$, for free-slip boundary conditions. A detailed study of the amplitude equations that could be written at this interaction point would be needed before any further blind exploration of the control space should be made with a costly spectral code. This is why only partial bifurcation diagrams have been displayed in the present work. Stability analysis of the square or hexagonal patterns also needs to be made.

Finally these investigations of zero- and very small-Prandtl-number convection could give a qualitative explanation of solar granulation. The observation of polygonal patterns in the connective zone of the sun is consistent with the present numerical experiments, regardless of the huge difference in the Rayleigh number ($R \sim 10^{11}$ for the sun). The intermittent behaviour of these structures could be explained by the competition between multiple metastable patterns.

I appreciated discussions with Stephan Fauve and Jack Herring during the course of this work. I thank Robert Kerr for helping me with use of his KER code and Hope Hamilton for a careful reading of the manuscript. This work was supported by the National Science Foundation through its contract with the National Center for Atmospheric Research (NCAR). The computations were performed on NCAR's CRAY Y-MP, with allocations provided by the Advanced Study Program and the Geophysical Turbulence Program of NCAR.

REFERENCES

BOLTON, E. W. BUSSE, F. H. 1985 Stability of convection rolls in a layer with stress-free boundaries. *J. Fluid Mech.* **150**, 487–498.

BOLTON, E. W., BUSSE, F. H. & CLEVER, R. M. 1986 Oscillatory instabilities of convection rolls at intermediate Prandtl numbers. *J. Fluid Mech.* **164**, 469–485.

BUSSE, F. H. 1967 On the stability of two-dimensional convection in a layer heated from below. *J. Math. Phys.* **46**, 140–150.

BUSSE, F. H. 1971 Stability regions of cellular flow. In *Instability of Continuous Systems* (ed. H. Leipholz), pp. 41–47. Springer.

BUSSE, F. H. 1972 The oscillatory instability of convection rolls in a low Prandtl number fluid. *J. Fluid Mech.* **52**, 97–112.

BUSSE, F. H. 1978 Nonlinear properties of convection. *Rep. Prog. Phys.* **41**, 1929–1967.

BUSSE, F. H. 1981 Transition to turbulence in Rayleigh-Bénard convection. In *Hydrodynamics Instabilities and the Transition to Turbulence* (ed. H. L. Swinney & J. P. Gollub) pp. 97–137. Springer.

BUSSE, F. H. 1989 Fundamentals of thermal convection. In *Mantle Convection, Plate Tectonics and Global Dynamics* (ed. W. R. Peltier), pp. 23–95. Gordon and Breach.

BUSSE, F. H. & BOLTON, E. W. 1984 Instabilities of convection rolls with stress-free boundaries near threshold. *J. Fluid Mech.* **147**, 115–125.

BUSSE, F. H. & CLEVER, R. M. 1979 Instabilities of convection rolls in a fluid of moderate Prandtl number. *J. Fluid Mech.* **91**, 319–335.

BUSSE, F. H. & CLEVER, R. M. 1981 An asymptotic model of two-dimensional convection in the limit of low Prandtl number. *J. Fluid Mech.* **102**, 75–83.

BUSSE, F. H. & SIEBER, M. 1991 Regular and chaotic patterns of Rayleigh-Bénard convection. In *Bifurcation and Chaos: Analysis, Algorithms, Applications* (ed. R. Seydel, F. W. Schneider, T. Küppers and H. Trogen). International Series of Numerical Mathematics vol. 97, pp. 79–92. Basel: Birkhäuser.

CHANDRASEKHAR, S. 1961 *Hydrodynamic and Hydromagnetic Stability*. Clarendon.

CHIFFAUDEL, A., FAUVE, S. & PERRIN, B. 1987 Viscous and inertial convection at low Prandtl number: Experimental study. *Europhys. lett.* **4**, 555–560.

CLEVER, R. M. & BUSSE, F. H. 1974 Transition to time-dependent convection. *J. Fluid Mech.* **65**, 625–645.

CLEVER, R. M. & BUSSE, F. H. 1978 Large wavelength convection rolls in low Prandtl number fluid. *Z. Angew. Math. Phys.* **29**, 711–714.

CLEVER, R. M. & BUSSE, F. H. 1981 Low-Prandtl-number convection a layer heated from below. *J. Fluid Mech.* **102**, 61–74.

CLEVER, R. M. & BUSSE, F. H. 1987 Nonlinear oscillatory convection. *J. Fluid Mech.* **176**, 403–417.

CLEVER, R. M. & BUSSE, F. M. 1989 Nonlinear oscillatory convection in the presence of a vertical magnetic field. *J. Fluid Mech.* **201**, 507–523.

CLEVER, R. M. & BUSSE, F. H. 1990 Convection at very low Prandtl numbers, *Phys. Fluids* A**2**, 334–339.

CRAWFORD, J. D. & KNOBLOCH, E. 1991 Symmetry and symmetry-breaking bifurcations in fluid dynamics. *Ann. Rev. Fluid Mech.* **23**, 341–387.

CROQUETTE, V. 1989*a* Convective pattern dynamics at low Prandtl number: Part I. *Contemp. Phys.* **30**, 113–133.

CROQUETTE, V. 1989*b* Convective pattern dynamics at low Prandtl number: Part II. *Contemp. Phys.* **30**, 153–171.

CROSS, M. C. 1980 Derivation of the amplitude equation at the Rayleigh–Bénard instability. *Phys. Fluids* **23**, 1727–1731.

DANIELS, P. G. & ONG, P. G. 1990 Nonlinear convection in a rigid channel uniformly heated from below. *J. Fluid Mech.* **215**, 503–523.

FAUVE, S., BOLTON, E. W. & BRACHET, M. E. 1987 Nonlinear oscillatory convection: A quantitative phase dynamics approach. *Physica* D**29**, 202–214.

FRISCH, U., SHE, Z. T. & THUAL, O. 1986 Viscoelastic behaviour of cellular solutions to the Kuramoto–Sivashinsky model. *J. Fluid Mech.* **168**, 221–240.

GOLUBITSKY, M., STEWART, I. & SCHAEFFER, D. G. 1988 *Singularities and Groups in Bifurcation Theory*, vol. II, Chap. xvii. Springer.

GOLUBITSKY, M., SWIFT, J. W. & KNOBLOCH, E. 1984 Symmetries and pattern selection in Rayleigh-Bénard convection. *Physica* D**10**, 249–276.

HERRING, J. R. 1970 Convection at zero Prandtl number. *Woods Hole Oceanogr. Inst. Tech. Rep. WHOI*-70-01.

HERRING, J. R. 1987 Moment closure for thermal convection : A viable approach ? In *The Internal Solar Angular Velocity* (ed. B. R. Durney and S. Sofia), pp. 275–288. D. Reidel.

JONES, C. A., MOORE, D. R. & WEISS, N. O. 1976 Axisymmetric convection in a cylinder. *J. Fluid Mech.* **73**, 353–388.

KRAICHNAN, R. H. & SPIEGEL, E. A. 1962 Model for energy transfer in isotropic turbulence. *Phys. Fluids* **5**, 583–588.

LIPPS, F. B. 1976 Numerical simulation of three-dimensional Bénard convection in air. *J. Fluid Mech.* **75**, 113–148.

MALKUS, W. V. R. & VERONIS, G. 1958 Finite amplitude convection. *J. Fluid Mech.* **4**, 225–260.

MCLAUGHLIN, J. B. & ORSZAG, S. A. 1982 Transition from periodic to chaotic thermal convection. *J. Fluid Mech.* **122**, 123–142.

MENEGUZZI, M., SULEM, C., SULEM, P. L. & THUAL, O. 1987 Three-dimensional numerical simulation of convection in low Prandtl number fluid. *J. Fluid Mech.* **182**, 169–191.

MOORE, D. R. & WEISS, N. O. 1973 Two-dimensional Rayleigh–Bénard convection. *J. Fluid Mech.* **58**, 289–312.

MOSER, R. D., MOIN, P. & LEONARD, A. 1983 A spectral numerical method for the Navier–Stokes equations with application to Taylor–Couette flow. *J. Comput. Phys.* **52**, 524–544.

NEWELL, A. C., PASSOT, T. & SOUL, M. 1990 The phase diffusion and mean drift equations for convection at finite Rayleigh numbers in large containers. *J. Fluid Mech.* **220**, 187–252.

NEWELL, A. C. & WHITEHEAD, J. A. 1969 Finite bandwidth, finite amplitude convection. *J. Fluid Mech.* **38**, 279–303.

PROCTOR, M. R. 1977 Inertial convection at low Prandtl number. *J. Fluid Mech.* **82**, 97–114.

SCHLÜTER, A., LORTZ, D. & BUSSE, F. H. 1965 On the stability of steady finite amplitude convection. *J. Fluid Mech.* **23**, 129–144.

SEGEL, L. A. 1969 Distant side-walls cause slow amplitude modulation of cellular convection. *J. Fluid Mech.* **38**, 203–224.

SIGGIA, E. D. & ZIPPELIUS, A. 1981 Pattern selection in Rayleigh-Bénard convection near threshold. *Phys. Rev. Lett.* **47**, 835–838.

SPIEGEL, E. A. 1962 Thermal turbulence in a very small Prandtl number. *J. Geophys. Res.* **67**, 3063–3070.

SPIEGEL, E. A. & VERONIS, G. 1960 On the Boussinesq approximation for a compressible fluid. *Astrophys. J.* **131**, 442–447.

SULEM, P., SULEM, C. & THUAL, O. 1985 Direct numerical simulation of three-dimensional convection in liquid metals. *Prog. Astro. Aeronaut.* **100**, 125–151.

TVEITEREID, M., PALM, E. & SKOGVANG, A. 1986 Transition to chaos in Rayleigh-Bénard convection. *Dyn. Stab. Syst.* **1**, 343–365.

VERONIS, G. 1966 Large-amplitude Bénard convection. *J. Fluid Mech.* **26**, 49–68.

WU, W. S., LILLY, D. K. & KERR, R. M. 1991 Helicity and thermal convection wide shear. *J. Atmos. Sci.* (submitted).

ZIPPELIUS, A. & SIGGIA, E. D. 1982 Disappearance of stable convection between free-slip boundaries. *Phys. Rev.* A**26**, 1788–1790.

ZIPPELIUS, A. & SIGGIA, E. D. 1983 Stability of finite-amplitude convection. *Phys. Fluids* **26**, 2905–2915.